Additive Manufacturing 37 (2021) 101647

Contents lists available at ScienceDirect

Additive Manufacturing

journal homepage: www.elsevier.com/locate/addma

Research Paper

Multi-material additive manufacturing of functionally graded carbide ceramics via active, in-line mixing

Joshua S. Pelz [a,b], Nicholas Ku [b], William T. Shoulders [b], Marc A. Meyers [a], Lionel R. Vargas-Gonzalez [b,*]

[a] University of California, San Diego, La Jolla, CA 92093, United States
[b] U.S. Army Combat Capabilities Development Command Army Research Laboratory, Weapons and Materials Research Directorate, Aberdeen Proving Ground, Aberdeen, MD 21005-5069, United States

ARTICLE INFO

Keywords:
Material extrusion
Heterogeneous
Active mixing
Carbides
Functional grading

ABSTRACT

Advanced ceramics are required in many applications including armor, engine components, and wear parts for abrasive, corrosive, and high temperature environments. Heterogeneous structuring in these materials has the potential to unlock extrinsic mechanisms that improve damage tolerance, of vital importance for structural functionality. However, traditional ceramic powder processing and forming techniques limit the design space to simple geometries with chemically homogenous microstructures. Thus, additive manufacturing by direct ink writing (DIW) was applied to fabricate multi-phase carbide specimens with tailored composition and meso-structure. A custom DIW system was developed to allow simultaneous extrusion and mixing of multiple inks, comprised of ceramic particulate suspensions, through a single nozzle. Boron carbide (B_4C) and silicon carbide (SiC) were chosen for this study due to their excellent mechanical properties. Aqueous B_4C and SiC inks were loaded to 47.5 vol% ceramic content and showed yield-pseudoplastic behavior. The carbide inks were characterized and modified to exhibit similar rheological behavior (yield stress and viscosity), and were used to produce B_4C–SiC parts with either discrete or continuous composition variation. Specimens were hot pressed at 35 MPa and 1950 °C, yielding near full density with hardness (Knoop) values of 20–23 GPa. Tailored heterogeneity, achieved via active in-line mixing, is revealed through microstructural characterization. Cracking observed in the specimen with discretely varied composition is the result of thermally-induced residual stress, and is elucidated through analytical calculations.

1. Introduction

1.1. Motivation and background

Ceramic body armor has a long history in the U.S. Military and has been actively developed for many decades. A wide array of ceramic materials has been explored, with boron carbide (B_4C) and silicon carbide (SiC) most often used due to their high hardness and low density [1]. This continuous effort has led to highly engineered, lightweight material systems with unparalleled protective capabilities. However, while these monolithic ceramic specimens have approached the limits of hardness and strength, which are key properties for projectile defeat, cracking is eventually the dominant failure mechanism at higher projectile velocities [2]. As a result, the mode of fragmentation has the greatest effect on ballistic resistance [3]; the most effective way to improve ballistic performance is to increase the energy of fracture. Achieving full, theoretical density by reducing defects leads, generally, to superior mechanical properties [4]. Following this logic, traditional knowledge tells us to produce ceramic armor to be fully dense and of a single, monolithic material. While it is true that reducing defects, such as

Abbreviations: B_4C, boron carbide; SiC, silicon carbide; AM, additive manufacturing; DIW, direct ink writing; BET, Brunauer–Emmett–Teller; PEI, polyethyleneimine; MC, methylcellulose; HCl, hydrochloric acid; FFF, fused filament fabrication; SEM, scanning electron microscope; EDS, energy dispersive spectroscopy; XRD, X-ray diffractometer; vol%, volume fraction; CNC, computer numerical control; T_j, joining temperature; CTE, coefficient of thermal expansion; HK2, Knoop hardness with 2 kgf load; ISE, indentation size effect.

* Corresponding author.
E-mail addresses: jpelz@eng.ucsd.edu (J.S. Pelz), nicholas.ku.civ@mail.mil (N. Ku), william.t.shoulders2.civ@mail.mil (W.T. Shoulders), mameyers@eng.ucsd.edu (M.A. Meyers), lionel.r.vargas-gonzalez.civ@mail.mil (L.R. Vargas-Gonzalez).

https://doi.org/10.1016/j.addma.2020.101647
Received 22 June 2020; Received in revised form 26 August 2020; Accepted 30 September 2020
Available online 7 October 2020
2214-8604/Published by Elsevier B.V.

porosity, is vital to unlock the high hardness and compressive strength of ceramics, there is still the issue of penetration by fragmentation during ballistic events. For this reason, alternative methods of fracture mitigation must be explored to fully realize the exceptional properties of advanced ceramics.

1.2. Natural design motifs

Inspiration for alternative methods of fracture mitigation can be gained from nature, where biological structures derive superior mechanical performance using hierarchical structuring and composition gradients, with one typical example being the nacreous abalone shell. Nacre is a natural composite of calcium carbonate tiles and organic interlayers in a 'brick and mortar' microstructure with additional higher-scale organic mesolayers [5]. The structural organization of nacre at multiple length-scales leads to an 8-fold increase in fracture toughness over that of pure calcium carbonate [6]. Similarly, fish scales, such as those of the arapaima, use hierarchical structuring and mineralization gradients to increase toughness, strength, and ductility while remaining thin and lightweight [7,8]. Fig. 1 highlights two biological design motifs, layering and mineral gradients, which are found in arapaima scales and the abalone shell.

Bioinspired design features can enhance performance if integrated into next-generation ceramic armor materials since they can provide greater strength, hardness, and toughness [9]. Indeed, recent studies have shown that ceramic specimens with second phase inclusions, layers, and multi-scaled organization show an increased toughness due to extrinsic fracture mechanisms that inhibit crack propagation [10–14]. Moshtaghioun et al. [10] observed two extrinsic toughening mechanisms, crack tip deflection and crack bridging, for a B_4C matrix with SiC inclusions. These extrinsic toughening mechanisms led to a 65% increase in toughness compared with monolithic B_4C. Wang et al. [11] and Wilkerson et al. [12] demonstrated the toughening effect of using biomimetic nacre-like structures in ceramic composites. Rao et al. [13] and Lugovy et al. [14] increased the toughness of layered ceramic materials using thin compressive layers to deflect cracks at layer interfaces. These findings have catalyzed a major research effort to study the effects of composition, geometry, and multi-scaled structuring on mechanical performance in ceramic materials.

1.3. Fabrication methods for heterogeneous structures

To manufacture these multi-phase materials, a processing technique is required that can produce complex, three-dimensional parts with material heterogeneity and organization across multiple length scales. Various ceramic forming technologies exist and are of commercial manufacturing scale, e.g. pressing, extrusion, slip casting, tape casting, and injection molding [15]. However, these techniques severely limit the available design space for variation of composition and geometry. Tape casting, without secondary layering steps, only allows control of the sheet thickness [15]. Pressing and extrusion produce parts of simple geometry such as disks, rods, and tubes [15]. Slip casting and injection molding afford the most geometric freedom, but do not enable material heterogeneity [16]. With the exception of layered tape-cast specimens, where layers may be of different materials [17], these techniques produce chemically homogenous parts.

Additive manufacturing (AM), on the other hand, enables the production of parts with complex, multi-scaled geometries, including internal structures [18–20]. Additionally, multi-material AM can support material heterogeneity by discrete layers and composition gradients [12,21]. Direct ink writing (DIW), a material extrusion AM technique [22] that allows multi-material and mixing capabilities [23–26], was chosen to fabricate multi-phase carbide specimens in this study. The DIW technique, also known as robocasting, involves extrusion of a line of highly-loaded colloidal suspension, termed 'ink', through a nozzle in a specific pattern layer-by-layer to produce a three-dimensional part [27]. This line of deposited material is known as a trace. The ink used for DIW relies on yield-pseudoplastic behavior to self-support following extrusion. Yield-pseudoplastic rheology enables the ink to retain structural integrity up to its yield stress, followed by shear-thinning behavior [28,29]. This behavior is critical for ink to both flow through a small nozzle (high-shear environment) and retain its shape post-extrusion (low-shear environment).

1.4. Ceramic additive manufacturing

Ceramic AM techniques are defined as indirect processes, because post-processing is required to densify printed green bodies [22]. A prerequisite of high sintered density is high green density; this requires high ceramic content and low binder/dispersant content [30]. The maximum density of loose, random packing for powder is approximately 60 vol% [31], which effectively sets the upper-bound for ceramic

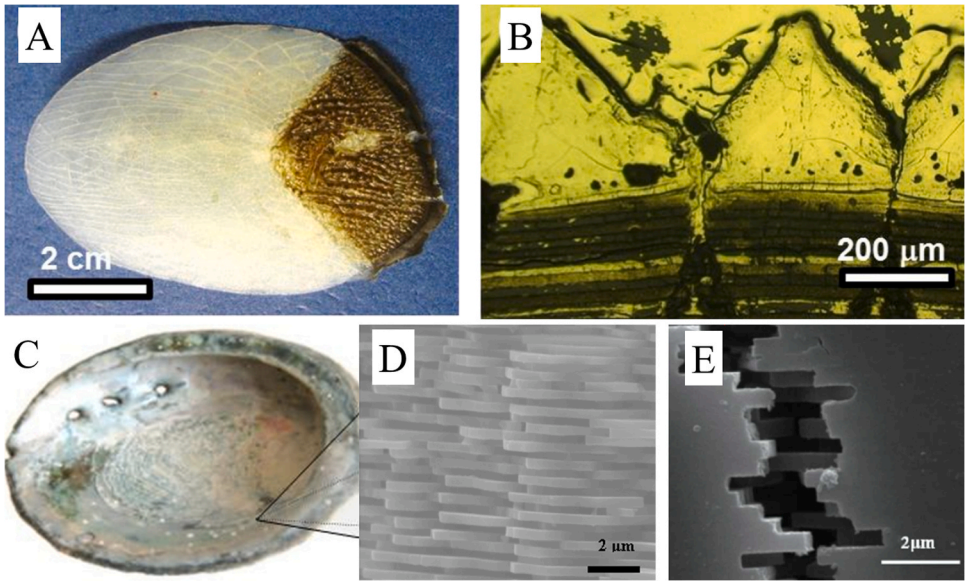

Fig. 1. (A) The arapaima scale consists of a flexible base and hard, mineralized outer surface that inhibits penetration. (B) The mineralization gradient from the base layers to the hard, top surface arrests cracks that form in the arapaima scale during penetration events. (C) The abalone shell uses layering and hierarchical structuring to improve toughness over its weak constituent materials. (D) $CaCO_3$ tiles are arranged in a brick and mortar structure. (E) The tortuous crack path around aragonite tiles leads to an 8-fold increase in the toughness of nacre over pure $CaCO_3$ [6].

content. Ink formulation in this study targets a ceramic content as close to 60 vol% as possible without sacrificing yield-pseudoplastic rheology. Shrinkage occurs during sintering as a function of ceramic content and can impart significant residual stresses on densified parts. Residual stresses are the result of non-uniform shrinkage, which can arise from asymmetrical geometries and chemical heterogeneity. This effect is especially pronounced in parts with discrete composition changes, such as layered composites, where different coefficients of thermal expansion (CTE) produce compressive and tensile residual stresses that can lead to part failure [32]. Thus, a balance must be found between printability and post-print processing, namely sintering behavior.

Dense, complex oxide ceramic parts have been produced via AM techniques [33–37], whereas AM of dense carbides has faced challenges due to difficult colloidal dispersion and high sintering temperatures. Costakis et al. [38] produced B_4C parts via material extrusion, but obtained a theoretical density of just 82% through pressureless sintering. A higher theoretical density of 95% was achieved for extruded B_4C parts by Eqtesadi et al. [39], but required the use of cold isostatic pressing and spark plasma sintering. These studies demonstrated the feasibility of AM for producing dense, geometrically complex carbide parts, but lacked investigation into material heterogeneity.

Several recent studies have attempted multi-material ceramic AM in order to develop functionally graded oxides. Functionally graded oxide ceramics were made using a material extrusion process with active mixing by Li et al. [24]. Similarly, a material extrusion system with mixing capabilities was designed by Smay et al. [23] to develop ternary mixtures for high-throughput characterization of oxide ceramics. Bio-inspired ceramic-metal composites were demonstrated by Wilkerson et al. [12] with discrete "brick and mortar" structures mimicking the abalone nacre. These bioinspired $0.95Al_2O_3$–0.05Ni composites showed improved toughness compared with pure alumina based on their functional design. Studies on AM of functionally graded ceramics often use custom-built equipment due to the lack of commercial systems with multi-material and mixing capabilities [12,23,24]. Whereas multi-material ceramic AM of oxides has seen recent progress, fabrication of functionally graded carbides has remained elusive due to challenges with densification, ink formulation, and sourcing processing equipment.

This study intends to fill the gap in available processing technologies for the development of functionally graded carbide materials with tailored structural organization and material heterogeneity. High ceramic content B_4C and SiC inks are formulated with suitable rheology and their printability is evaluated. A custom, low-cost DIW system is designed with active, in-line mixing capabilities for real-time control of material heterogeneity. Characterization of multi-phase carbide specimens in both green and sintered states is performed to demonstrate and validate the effectiveness of this processing technique.

2. Experimental procedures

A custom DIW system was developed to enable the printing of carbide components with heterogeneous structuring. Boron carbide and silicon carbide powders were suspended as aqueous inks and used as the feedstock for printing heterogeneous carbide specimens. The custom DIW system was assessed for its ability to print and mix multiple materials at specified ratios. Printed specimens were tested for shape retention, density, microstructure, and mechanical properties to elucidate the advantages and limitations of our ceramic AM method.

2.1. Feedstock preparation

B_4C (mean particle size ~ 0.8 μm, ESK Tetrabor 3000F B_4C, Kempten, Germany) and SiC (mean particle size ~ 0.7 μm, Superior Graphite 490N SiC, Chicago, IL) powders were processed into high ceramic content aqueous ink formulations, with rheological behavior controlled using mixtures of organic binders and dispersants. Brunauer–Emmett–Teller (BET) particle surface area was measured using a Micromeritics Tristar II Plus (Norcross, GA). The B_4C ink contained polyethyleneimine (25 kDa PEI, Sigma-Aldrich, Louis, MO), hydrochloric acid (96.99% HCl, Sigma-Aldrich, Louis, MO), methylcellulose (4000cP MC, Sigma-Aldrich, Louis, MO), and deionized water. The SiC ink contained of polyethyleneimine (25 kDa PEI, Sigma-Aldrich, Louis, MO), methylcellulose (4000cP MC, Sigma-Aldrich, Louis, MO), and deionized water.

A stock solution of 5 vol% methylcellulose (MC) and deionized water was made to simplify processing at the time of mixing. Four grams of MC powder were slowly added to 80 mL of deionized water at 95 $\bar{7}$C on a mixing hot-plate. Once all MC powder was dissolved, the solution was placed into an ice-bath until it became clear, signifying gel-network formation [40].

Ink formulations were mixed in 120 g batches using a DAC 400 VAC SpeedMixer (Flacktek, Landrum, SC). PEI and one-half of the ceramic powder were added to a 150 g Flacktek container and mixed at 800, 1200, and 1600 RPM steps for times of 30, 30, and 15 s, respectively. Next, using the same mixing procedure twice, the deionized water and HCl were incorporated into the Flacktek container along with small amounts of ceramic powder. The MC solution and remaining ceramic powder were then added into the Flacktek container and mixed with 800, 1200, 1600, and 2000 RPM steps for times of 60, 60, 30, and 15 s, respectively, to be homogenized. The three rough mixing stages and final homogenizing mixing stage resulted in a total mixing time of 7 min and 45 s. SiC ink formulation follows the same procedure as the B_4C ink, with the exclusion of the HCl addition, as no further modification of particle surface charge is necessary to attain dispersion.

2.2. Rheology

Rheological characterization of inks was performed using an MCR 302 (Anton Paar, Graz, Austria). A concentric cylinder fixture with a nominal diameter of 27 mm and a gap of 1 mm was used for testing of the ceramic inks. A damp paper towel was placed at the top of the concentric cylinder apparatus to reduce water loss during testing. Rheological testing was conducted at a controlled temperature of 25 °C. Samples were pre-sheared after loading at 30 s^{-1} for 60 s and allowed to equilibrate for 5 min before testing to remove shear history from the sample. The viscosity was measured with a continuous flow test from 0.1 to 100 s^{-1}.

2.3. Direct ink writing

Carbide parts were formed via DIW using a custom-built system, depicted in Fig. 2, with multi-material and in-line mixing capabilities [41]. This system has two primary modules, the print head and the feed system, and interfaces with a low-cost fused filament fabrication (FFF) 3D printer (LulzBot Taz 6, Aleph Objects, Loveland, CO). The feed system consists of two units, which are independently controlled to output two different ceramic inks to the print head. Each unit utilizes a lead-screw driven plunger for precise, volumetric feed rate control. Ceramic ink is fed through 4 mm inner-diameter Teflon tubes to the print head, which contains an auger to enable in-line mixing and precise extrusion. The auger, depicted in Fig. 2C, provides shear mixing to blend highly viscous inks, which tend to resist turbulent flow and are therefore difficult to mix with impellers or other turbulent dispersion methods. The mixed ink is extruded through the 1.2 mm orifice of the nozzle. The Taz 6 3D printer serves as the 3-axis motion system, allowing for either FFF of plastic parts using the provided tool head or DIW of ceramic specimens using the custom-made print head and feed system. In fact, several components of the print head and feed system were printed from ABS filament (Chroma Strand Labs, Loveland, CO) and PC-ABS filament (Proto-pasta, Vancouver, WA) using the Taz 6 with its FFF tool head. The Taz 6 was selected due to its suitable precision, print volume, and open-source design, and its firmware was modified to remove temperature related errors, print head spatial variations, and custom tool path

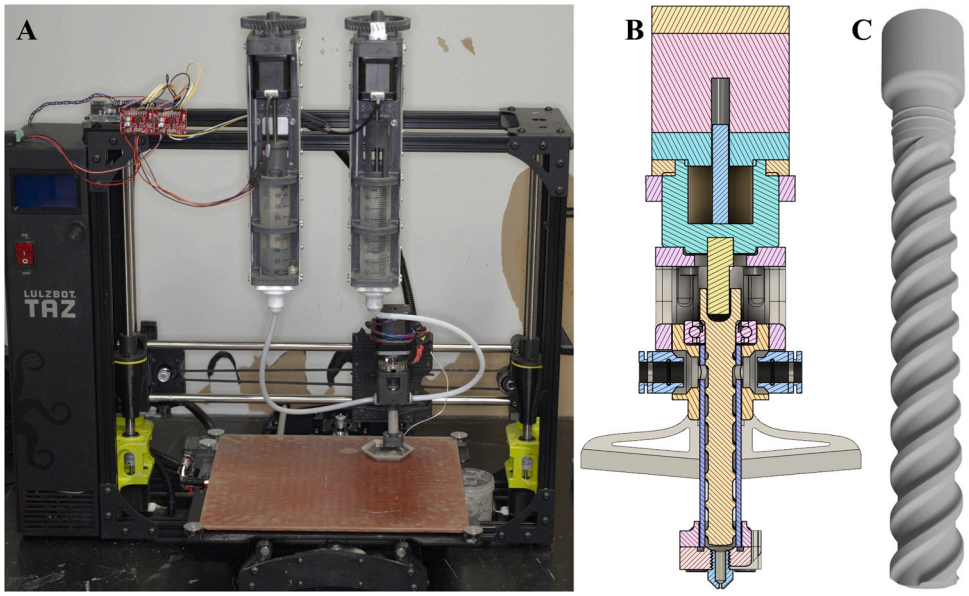

Fig. 2. (A) The DIW system consists of two feed system units, the feed system controller, and the print head mounted on a LulzBot Taz 6 printer. (B) Cross-section view of the print head illustrating the mechanisms involved in mixing and extrusion. (C) The auger uses a series of channels to provide high-shear mixing and consistent material extrusion.

modifications.

Slic3r (https://slic3r.org/), a 3D slicing engine, was used to prepare the G-code sent to the Taz 6. Relevant slicing parameters include a 1.2 mm layer height, 1.2 mm trace width, and print speed of 5 mm/s. The 1.2 mm trace width is determined by the nozzle width of 1.2 mm. The 1.2 mm layer height was chosen to reduce nozzle dragging effects (observed for lower layer heights), while maintaining acceptable print quality. At layer heights greater than 1.2 mm, print quality was visually reduced as extruded material tended to deflect sideways before contacting the previous layer. A conservative print speed of 5 mm/s was selected to reduce under-extrusion, visually observed as thinner traces with gaps in between, which tended to occur at higher speeds.

Composition was controlled automatically using G-code, whereby commands were sent to the feed system to adjust feed rate and ratio. Feed system unit 0 was loaded with B_4C ink and feed system unit 1 was loaded with SiC ink. The G-code composition command uses an 'R' identifier followed by a 0.00–1.00 value to denote composition changes of any ratio as a function of vol% SiC. For example, R0.25 would adjust the feed ratio to 75 vol% B_4C and 25 vol% SiC. A purge operation was used during compositional changes. The purge operation moves the print-head over a waste container, located beside the build platform, and extrudes a specified volume of material to clear any remaining ink of the prior composition from the print head. Prior to printing, 'R' identifier commands were manually added to the G-code files used for printing heterogeneous parts, with the purpose of commanding composition changes at the correct locations. Carbide specimens with composition variation in the build direction were printed onto acrylic squares, which were mounted on the Taz 6 build platform. Directly after each print completed, the acrylic squares were moved to a chamber, which allowed the specimens to dry in a controlled environment. The chamber was set to 77% relative humidity and ambient temperature. Printed carbide specimens were dried for 48 h.

In order to calculate the purge volume, different colors of Play-Doh were printed in zig-zag formations using the same printing parameters. The trace length required to fully change Play-Doh color following a composition change was measured from a photograph of the zig-zag print. Trace length was converted to volume by assuming a cylindrical geometry with a diameter of 1.2 mm. Play-Doh was used as a surrogate for the ceramic ink due to its superior optical contrast, ease of acquisition, and similar yield-pseudoplastic behavior.

2.4. Printability

The printability of the carbide inks was determined by three tests. First, ink formulations were continuously extruded through nozzle orifice diameters of 0.6, 0.8, 1.0, and 1.2 mm in a purge operation to verify no clogging would occur during a print. Second, a single wall of stacked traces was printed, allowed to dry, and total height loss was measured. Total height loss is the difference of the measured height of the stacked traces from the nominal height, which is equal to the programmed layer height multiplied by the number of layers. Third, after drying, the total height loss was calculated for the heterogeneous carbide specimens.

2.5. Sintering and characterization

Two heterogenous B_4C–SiC specimens, one with discrete composition variations and one with a continuous composition variation along the build direction, were both (1) pyrolyzed by ramping at 1 7¯C/min up to 650 7¯C and holding for 24 h and (2) densified through hot pressing. The specimens were hot pressed at 35 MPa and 1950 °C for 2 h, using a 25 °C/min ramp rate and including an intermediate hold at 1350 °C for 1 h to volatilize oxide species. Density was determined using the Micromeritics GeoPyc Model 1360 (Norcross, GA). The GeoPyc determines density through displacement of a highly flowable, uniform-packing powder bed. This allowed for a true envelope density of the sample to be measured, which included both open and closed porosity in the sample volume. Densities were reported as a percentage of theoretical density, which was calculated using a rule of mixtures with values of 2.52 g/cc for boron carbide and 3.21 g/cc for silicon carbide [1]. Hot pressed specimens were cross-sectioned, mounted in epoxy, and polished using diamond media. Rough polishing was accomplished using a 125 μm diamond embedded disk until specimen surfaces were exposed and planar. Next, colloidal diamond suspensions of sizes 30, 9, and 3 μm were used to polish both specimens for times of 30, 30, and 90 min, respectively. A final polish was done using 1 and 0.25 μm colloidal diamond suspensions for times of 45 and 60 min, respectively. All polishing steps were performed at a 20 N load and with plate and head speeds of 300 and 150 RPM, respectively, in a co-rotating configuration. SEM micrographs were taken of the resulting polished cross-sections (FEI Apreo SEM, Hillsboro, OR). ImageJ was used for all

measurements on SEM micrographs [42]. Layer height, crack length, crack spacing, and crack opening displacement are reported from at least 25 measurements.

Knoop indentation was performed using a Wilson VH3100 automatic hardness tester (Buehler, Lake Bluff, IL). Indents were made at 2 kgf with a 10 s dwell and at sufficient spacing according to the ASTM C1326-13 standard [43]. An automatic grid pattern was used to create indents on the polished cross-sections of the discrete and continuous specimens. A 3 × 10 grid was used for the discrete specimen, with 10 indents each in the B_4C, SiC, and B_4C–SiC interface regions. A 5 × 36 grid was used for the continuous specimen, which allowed for 36 sampling locations of 5 measurements each along the build direction. Hardness data for the continuous specimen is reported as a function of distance along the build direction, starting from the B_4C-rich portion of the specimen.

3. Results and discussion

3.1. DIW system calibration

Communication between the Taz 6, which controls the print head, and the feed system is achieved using the I2C serial communication protocol. This provides a simple, yet effective, method for synchronizing the feed system and print head behavior via G-code, including the custom 'R' identifier to command feed ratio changes. Thus, for any point in 3-D space, the Taz 6 and feed system can communicate to adjust print speed, feed rate, and material composition. Mixing of the two ceramic inks requires a finite volume of material between the ends of the feed tubes and the nozzle tip, which results in a lag time between composition changes. Fig. 3 demonstrates the lag time between when a composition change is commanded and the actual change in composition of extruded material. A lag volume of 3.2 cm^3 was calculated by measuring the trace length required to fully change material color following a commanded change. During composition changes, the calculated lag volume is purged.

3.2. Ink rheology and printability

Ink formulations were developed with the goal of matching ceramic content and flow behavior across relevant shear rate regimes in order to maintain an optimal balance between printability and sinterability. High printability is defined by minimal slumping, which improves shape retention, and consistent extrusion. Increasing ceramic content and decreasing binder content improves the green density of printed parts, resulting in higher sinterability. Similarly, high surface area ceramic powder promotes densification during sintering but reduces printability.

Ceramic powder and aqueous binder/dispersant systems were characterized to determine which combination would provide the highest stability colloidal dispersion. BET measured surface areas for B_4C and SiC powders were 11.23 and 12.55 m^2/g, respectively. The surface area values and ceramic content were used to tailor various binder-dispersant systems. An exact binder-dispersant addition is necessary because colloid dispersion is improved until all particle surfaces are covered, with excess leading to pockets of agglomerated polymer that leave pores in sintered specimens. Polyethyleneimine (PEI) provided the most stable dispersion across a wide range of pH values for B_4C and SiC powders. Fig. 4A shows a plot of Zeta potential versus pH for the B_4C–PEI and SiC–PEI systems. Through the addition of PEI, carbide powders show optimal dispersion effects, defined as a Zeta potential value above 30 mV (absolute), in a wide pH range of 2–8. Ink formulations with lower sensitivity to pH variation have greater flexibility during the simultaneous extrusion of multiple inks.

Optimal formulations for B_4C and SiC were developed by varying ceramic and MC content to enable desired printability and maintain high ceramic content. The viscosities of notable formulations are plotted against shear rate in Fig. 4B to illustrate the effects of ceramic powder type and content and secondary binder content. All formulations show a significant decrease in viscosity with increasing shear rate, which is indicative of shear-thinning behavior. An increase from 47.5 to 50.0 vol % ceramic content while holding methylcellulose content at 1.0 vol% led to an increase in viscosity at all shear rates. Similarly, increasing the volume fraction of MC increased the viscosity at all shear rates. These relationships held true for all tested B_4C and SiC inks. SiC ink formulations at equivalent ceramic and MC content showed higher viscosities at all shear rates as compared with B_4C inks.

Final ink formulations for B_4C and SiC are reported in Table 1, with ceramic content constant at 47.5 vol% and MC contents of 5.0 and 2.5 vol%, respectively. Differences in powder morphology and surface chemistry between B_4C and SiC led to the difference in optimal methylcellulose content; the smaller SiC particle size of approximately 0.7 μm (compared to approximately 0.8 μm for the B_4C powder) leads to a higher influence of Van Der Waals forces, resulting in a greater tendency of soft agglomerate formation. Soft agglomerates increase viscosity and cause clogging. Carbide ink formulations reported in Table 1 were tested for consistent extrusion, and all tested nozzle sizes (0.6–1.2 mm) passed without clogging.

Multi-phase carbide parts were fabricated with the custom DIW system using the optimal ink formulations. To verify the printability of formulated inks, single stacked traces were printed and their shape retention was studied by comparing the expected and measured height of the traces. Fig. 5A highlights the shape retention capability of the B_4C ink, with less than 7% height loss from slumping for six stacked layers. As expected, because the flow behavior was matched, stacked traces printed with SiC ink show similar results with less than 9% height loss from slumping for six stacked layers. Stacked traces of a single wall

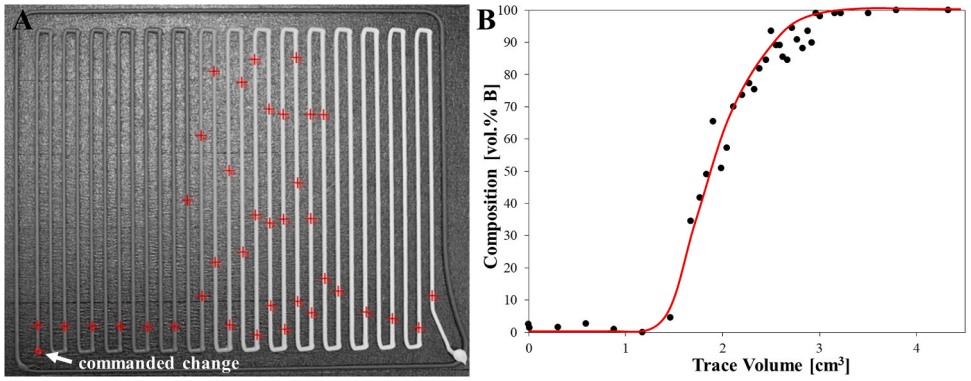

Fig. 3. (A) A single zig-zag trace was extruded to demonstrate composition adjustment in real-time. The composition was changed from 100% A (dark Play-Doh) to 100% B (light Play-Doh) at 'commanded change' point. (B) Gray-scale values were used to calculate composition values along the zig-zag, which were converted to volume by assuming a cylindrical geometry of diameter 1.2 mm. Play-Doh was used for this experiment because it provides higher optical contrast than carbide ink.

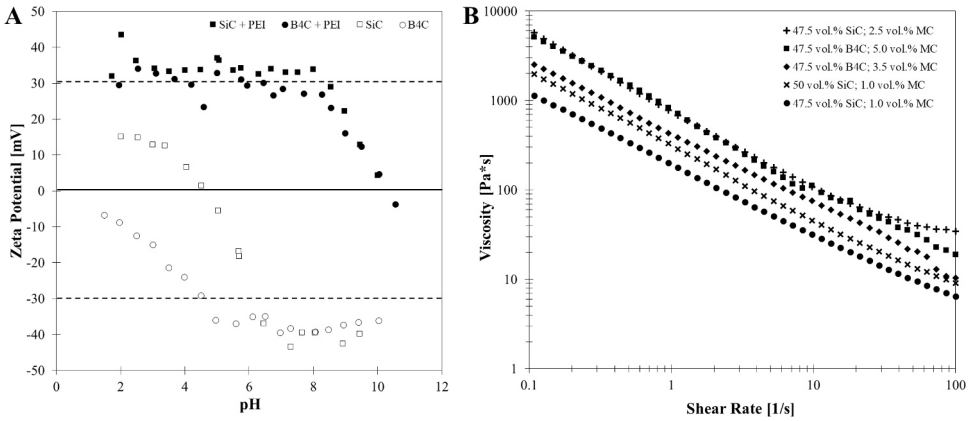

Fig. 4. (A) A zeta potential plot demonstrating the stabilizing effect of PEI additions to B_4C and SiC powders. (B) Rheological curves of SiC and B_4C inks illustrate their yield-pseudoplastic behavior. Viscosity is matched for + and ∎ formulations across a wide range of shear rates through the use of high viscosity methylcellulose.

Table 1
Final, optimized ink formulations used for direct ink writing of ceramic parts.

Ink type	Ceramic powder (vol %)	PEI (vol %)	HCl (vol %)	Water (vol%)	Methylcellulose (vol%)
SiC	47.50	3.00	–	47.00	2.5
B_4C	47.50	3.79	5.00	38.71	5

thickness set the upper-bound for height loss due to their large aspect ratio. To verify the printability of two inks simultaneously, cylindrical parts were printed while changing composition along the build direction in real-time. Fig. 5B shows the printing process for a discrete specimen, where composition is changed from pure B_4C to pure SiC and vise-versa, layer-by-layer. All specimens were printed at 100% infill using inside-out concentric patterns. Concentric infill was found to produce fewer defects than rectilinear patterns, where abrupt direction changes resulted in void formation between perimeter and infill traces. Cylinders of 25.4 mm diameter incorporating discrete and continuous composition variation were printed to nominal heights of 8.4 and 13.2 mm, respectively. After drying, the continuous specimen measured 12.87 mm in height, corresponding to a total height loss of 2.5%, and its external walls retained their vertical form. A similar height loss was measured for the discrete specimen.

3.3. Characterization of densified specimens

Macro specimen images in Fig. 6 demonstrate the novel multi-material capabilities of the custom DIW system, which uses active in-line mixing to tailor composition in real-time to any ratio of the two feed inks. Continuous and discrete specimens are shown in Fig. 6 in (A, C) green and (B, D) sintered states. In the green state, visually, B_4C shows up as dark gray and SiC shows up as tan. Fig. 6A shows the gradual transition in composition from B_4C (bottom layer) to SiC (top layer), whereas Fig. 6C shows discrete compositional changes layer to layer. Through the use of a humidity chamber, no drying-induced warpage or cracking was observed in the green specimens. No macroscopic pores were observed in the cross-sections of the dense parts. Based on the rule of mixtures of expected material feed during printing, densities of 99.2% and 98.6% of the theoretical value were calculated for the continuous and discrete B_4C–SiC specimens, respectively. The absence of macroscopic pores and ~ 50% linear shrinkage resulting from hot pressing indicate near full density and validate theoretical density calculations.

SEM micrographs of the cross-section of the discrete B_4C–SiC specimen in the sintered state are shown in Fig. 7. Micrographs were taken using the backscatter detector to highlight elemental contrast. B_4C and SiC phases show up as dark and light regions, respectively. B_4C and SiC layers were measured to be 549 ± 102 and 526 ± 95 micrometers, respectively. B_4C and SiC inclusions, dark and light spots, range in size from tens to hundreds of micrometers. These inclusions are the product of soft agglomerates that were not completely dispersed during in-line mixing of the ceramic inks. Printing pure SiC or B_4C is not possible as there will always be residual material inside the barrel and nozzle following a ratio change. Therefore, SiC layers are actually SiC-rich matrix regions with many pure SiC inclusions and a few pure B_4C inclusions. Similarly, B_4C layers are B_4C-rich matrix regions with many pure B_4C inclusions and a few pure SiC inclusions.

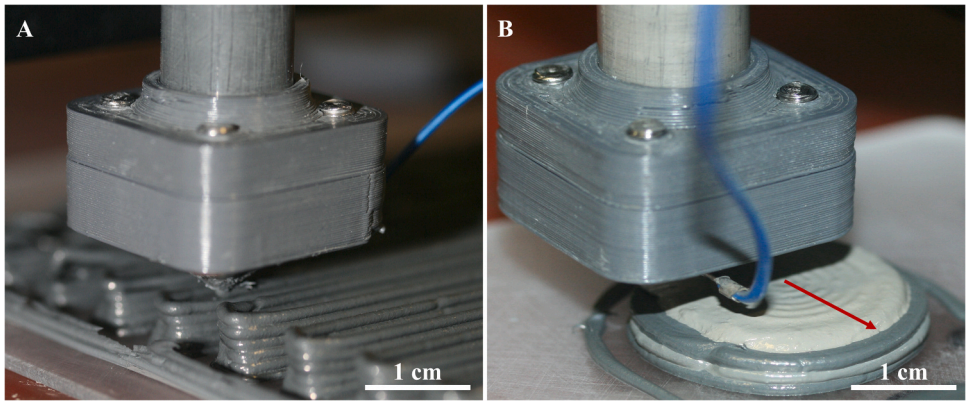

Fig. 5. (A) Stacked traces printed from the optimized B_4C ink demonstrate good shape retention post-extrusion and indicate a sufficient yield stress. (B) Inside-out concentric infill patterns were found to reduce printing related defects over rectilinear infill patterns.

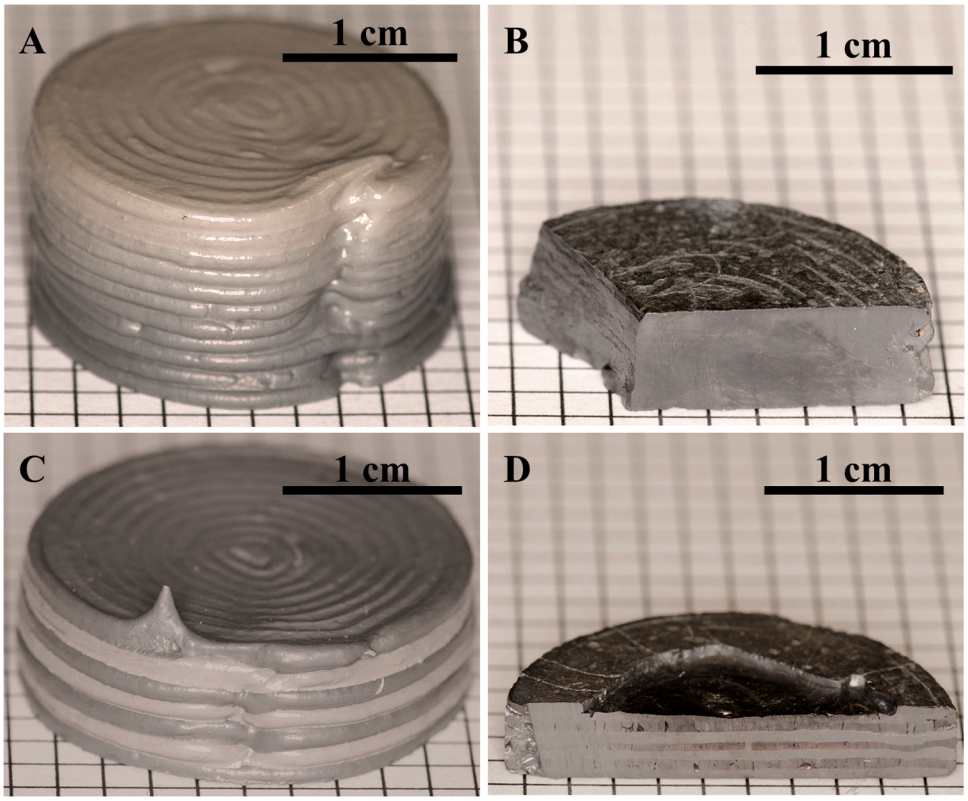

Fig. 6. A continuous carbide ceramic specimen produced via DIW in its (A) green and (B) sintered states. A discrete carbide ceramic specimen produced via DIW in its (C) green and (D) sintered states. Unidirectional shrinkages of approximately 50% in the build direction (bottom to top) resulted from the hot pressing process. Light and dark materials are SiC and B_4C, respectively.

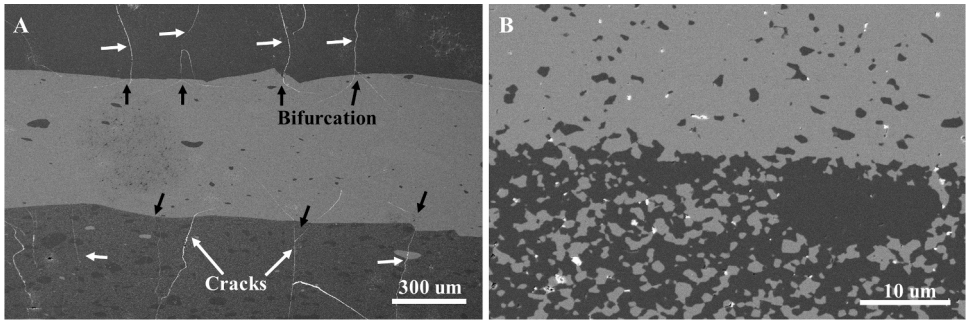

Fig. 7. SEM micrographs of the discrete B_4C–SiC specimen produced via direct ink writing. Dark material is B_4C and light material is SiC. B_4C and SiC inclusions appear as dark and light spots, respectively. Significant cracking is observed in B_4C layers.

Significant cracking seen in B_4C layers is likely due to the thermal expansion mismatch between B_4C ($5.5 * 10^{-6}$ K^{-1}) and SiC ($3.0 * 10^{-6}$ K^{-1}) [44]. These cracks occur preferentially within B_4C layers and are perpendicular to the interface. Cracks bifurcate and close as they traverse across layer interfaces into SiC layers. Interestingly, layer interfaces show good cohesiveness and no delamination is observed. The absence of cracking along layer interfaces may be the product of a limited amount of mixing that occurs between layers during the printing process. The small mixed zone, wherein the composition grades over a few micrometers, is shown in Fig. 7B.

SEM micrographs of the continuous specimen are shown in Fig. 8. In addition to the overall composition gradient, a gradient of inclusion distribution can be observed that follows the overall grading of composition. The number of B_4C and SiC inclusions decrease and increase, respectively, as the composition is graded from B_4C to SiC. White speckles seen in Figs. 7B and 8B are intergranular porosity. Minimal cracking can be seen originating from the SiC-rich surface of the continuous specimen in Fig. 8C. In contrast with the discrete specimen, the gradual composition change in the continuous specimen significantly reduced cracking. This finding is important in understanding how to tailor crack behavior and, ultimately, tune the fracture toughness of carbide materials through functional grading.

3.4. Analysis of stress and crack formation due to coefficient of thermal expansion mismatch

An analytical discussion of the mechanisms underlying the cracking seen in the discrete specimen is performed to provide a framework to inform future design of heterogenous parts with controlled residual stresses (σ_r) and fracture behavior. The approach used here follows one discussed by Meyers et al. [45], who evaluated two stress release mechanisms for Ti6Al4V–Al_3Ti laminate composites. First, creep can

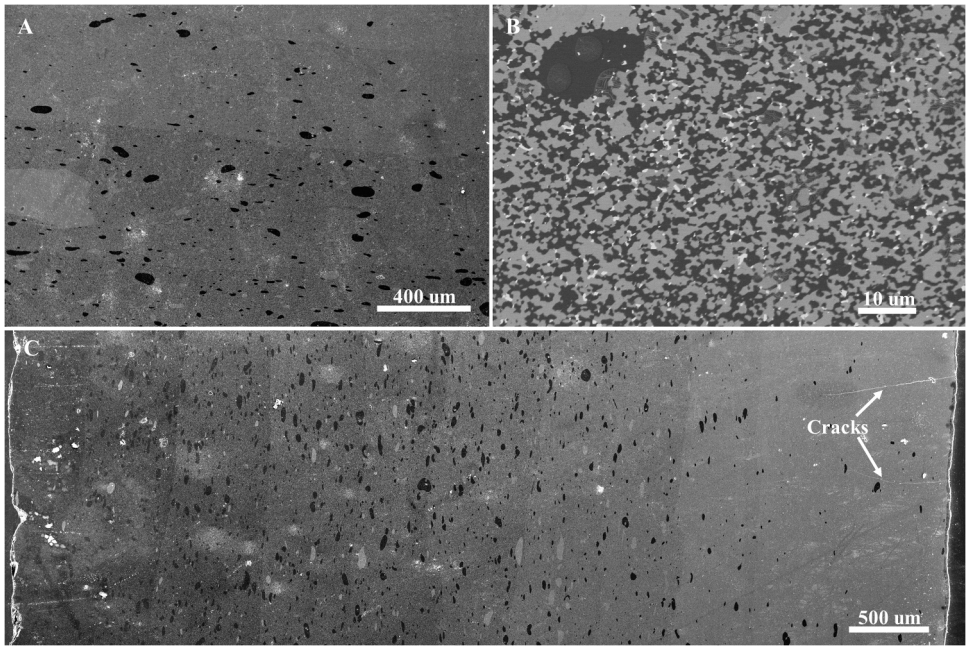

Fig. 8. SEM micrographs of the continuous B_4C–SiC specimen produced via direct ink writing. Dark material is B_4C and light material is SiC. B_4C and SiC inclusions appear as dark and light spots, respectively. It should be noted that micrograph (C) has been rotated clockwise 90° with respect to all other micrographs, which orients its build direction from left to right.

relieve residual stresses at temperatures above approximately half a material's melting temperature (T_m). Second, crack propagation relieves stresses below $\sim 0.5T_m$ as materials, generally, have higher fracture toughness at elevated temperatures above. Thus, creep is the dominant mechanism above $\sim 0.5T_m$ and crack propagation is the dominant mechanism below $\sim 0.5T_m$.

For ceramic materials, such as B_4C and SiC, creep occurs above the 'joining' temperature (T_j) and is assumed to release all σ_r generated above this temperature [46]. Creep becomes inactive as temperature drops below T_j. With this in mind, when calculating the residual stresses from coefficient of thermal expansion (CTE) mismatch, a zero-stress state is assumed for temperatures above T_j and that cracking is the dominant mechanism at temperatures less than T_j. The residual stresses of a layered composite with finite thickness and alternating brittle layers (of potentially different thickness) are:

$$\sigma_{r1} = \frac{E_1' E_2' f_2 (\alpha_2 - \alpha_1)\Delta T}{E_1' f_1 + E_2' f_2} \text{and} \quad (1)$$

$$\sigma_{r2} = \frac{E_1' E_2' f_1 (\alpha_1 - \alpha_2)\Delta T}{E_1' f_1 + E_2' f_2}, \quad (2)$$

where $E_i' = E_i/(1-\upsilon_i)$, $f_1 = \frac{l_1(N+1)}{2h}$, $f_2 = \frac{l_2(N-1)}{2h}$, E_i and ν_i are the elastic modulus and Poisson's ratio of component i, l_i is the layer thickness of component i, α_i is the CTE of component i, ΔT is the difference between T_j and ambient temperature, N is the total number of layers, and h is the total specimen height. B_4C and SiC are defined as component 1 and 2, respectively, T_j is equal to the sintering temperature of 1950 $\bar{7}$°C, ambient temperature is 25 °C, and N is 7. Fig. 9A defines relevant parameters used in this analysis and is simplified to only show one full B_4C layer and two partial SiC layers. The material properties used for the residual stress calculations of B_4C and SiC layers are shown in Table 2. The above equations and material properties are adapted from work by Orlovskaya et al. [44,46,47]. Layers are assumed to be pure B_4C and SiC in all calculations. The calculated residual stresses are −1.11 and +1.42 GPa for the B_4C and SiC layers, respectively, where tension and

Table 2
Material properties of carbides used to calculate residual stresses [44].

Component	E (GPa)	Poisson's ratio	CTE (10^{-6} K^{-1})
B_4C	483	0.17	5.5
SiC	411	0.16	3.0

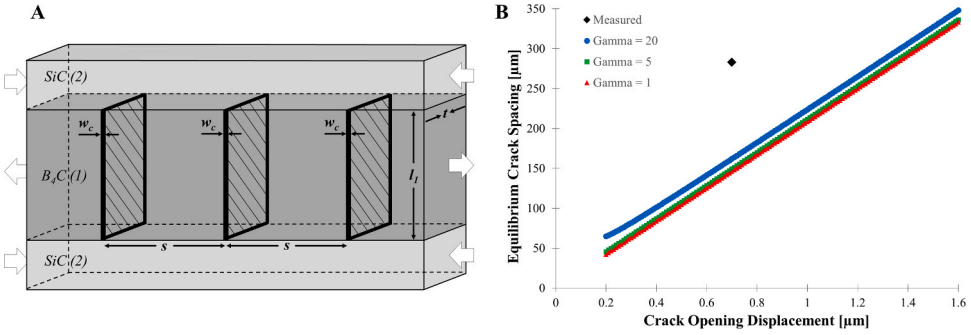

Fig. 9. (A) Diagram highlighting relevant parameters for the analysis of thermally-induced residual stresses, which shows one full B_4C layer and two partial SiC layers. (B) Plot of equilibrium crack spacing versus crack opening displacement for specific surface energies of $\gamma = 1$, $\gamma = 5$, and $\gamma = 20$.

compression are denoted by '−' and '+'. Based on these calculated residual stresses and the fact that the flexural strength of B_4C ranges from approximately 350 to 500 MPa [1,48,49], the B_4C layers should fracture. Indeed, these calculations are supported by microstructural observations, where cracks occur in tensile B_4C layers and then bifurcate and close as they traverse into compressive SiC layers.

Using Eqs. (1) and (2), residual stresses can be calculated as a function of the ratio l_1/l_2 to determine layer height configurations with lower residual tensile stresses. Tensile residual stresses in B_4C layers are inversely related to compressive residual stresses in SiC layers. Layer configurations that reduce tensile residual stress should maximize the l_1/l_2 ratio, which yields thick B_4C layers and thin SiC layers. Diminishing returns suggest an optimal layer thickness ratio at or slightly above 4.

Crack spacing (s) and crack opening displacement (w_c) for the discrete B_4C–SiC specimen were measured from SEM micrographs and found to have values of 283 ± 44 and 0.7 ± 0.3 μm, respectively. The equilibrium crack spacing can be estimated analytically by using an energy balance approach and making simplifying assumptions: strain energy is released by crack opening displacement and provides the energy for the creation of new surface area during crack formation. The surface energy per unit area of cracks is γ. Cracks are assumed to have a constant opening displacement, to be perpendicular to the layer interface, and to be arranged in a 2-dimensional network with equal spacing. Thus, the total strain energy (U_t) equals:

$$U_t = U_s + U_e, \tag{3}$$

where U_s is the increase in surface energy due to the creation of two new crack surfaces and U_e is the elastic strain energy due to tensile residual stress. The increase in surface energy is equal to:

$$U_s = t * l_1 * 2\gamma * n_c = l_1 * 2\gamma * t * \frac{2L}{s} = \frac{4\gamma}{s} * V, \tag{4}$$

where t is layer width, l_1 is layer thickness, and the number of cracks is n_c. The number of cracks equals $2L/s$, where L is layer length and the term $2/s$ represents the 2-dimensional network of cracks of spacing s. The total increase in surface energy per unit volume is then $4\gamma/s$ from Eq. (4). The elastic strain energy is:

$$U_e = \frac{\sigma_r^2}{2E^*} * l_1 * t * L = \frac{E^*\varepsilon^2}{2} * V, \tag{5}$$

where E^* is the effective elastic modulus of the layered structure and ε is the strain. Eq. (1) is adapted into elastic strain energy per unit volume in the following equation:

$$U_e = \frac{E^*\varepsilon^2}{2} = \frac{\frac{E_1' E_2' f_2}{E_1' f_1 + E_2' f_2}\left((\alpha_2 - \alpha_1)\Delta T + \frac{w_c}{s}\right)^2}{2}, \tag{6}$$

which accounts for elastic strain energy from both the CTE mismatch and the crack opening displacement by including w_c/s. The rationale for adding w_c/s to relax CTE mismatch strain is adapted from a methodology developed by Matthews and Blakeslee (1974), where misfit strain ε_m is relaxed by the displacement b (Burgers vector) and spacing s of misfit dislocations in the form $\varepsilon = \varepsilon_m + b/s$ [50,51]. By definition, ε_m and b/s must have different signs to cause stress relaxation, which holds true for our case where w_c/s and CTE mismatch strain are of different sign. According to the equilibrium theory of Van der Merwe (1972), the stable configuration can then be calculated by setting the derivative of U_t with respect to $1/s$ equal to zero [52]. Thus,

$$\frac{\partial U_t}{\partial 1/s} = 4\gamma + \frac{E^*\left(2w_c\left((\alpha_2 - \alpha_1)\Delta T + \frac{w_c}{s}\right)\right)}{2} = 0, \tag{7}$$

which can be modified to solve for equilibrium crack spacing

$$s = \frac{-E^* w_c^2}{4\gamma + E^* w_c(\alpha_2 - \alpha_1)\Delta T}. \tag{8}$$

The free surface energy for B_4C is approximately 3 J/m^2 [53,54]. Solving Eq. (8) using $\gamma = 3\ \frac{J}{m^2}$, $w_c = 0.7$ μm, $\Delta T = 1925$K, and material properties in Table 2, the equilibrium crack spacing is calculated as 148 μm; equilibrium being defined as all residual stress relieved by cracking. Thus, the difference between our calculated value and the measured value of 283 μm indicates residual stresses have not been fully relieved by cracking. Another likely factor in this difference is error in our crack opening displacement measurements. For example, if w_c is set to 1.5 μm, the equilibrium crack spacing is calculated as 314 μm. The sensitivity of equilibrium crack spacing to changes in crack opening displacement is demonstrated in Fig. 9B. The measured experimental value, represented as a diamond, is presented beside calculated curves for comparison. Surface energy seems to have a minimal effect on the equilibrium crack spacing, indicating the majority of the strain energy is released through crack opening displacement. Equilibrium crack spacing increases with increasing crack opening displacement and specific surface energy, resulting in fewer cracks.

3.5. Hardness testing

Reported hardness values in the literature for monolithic B_4C and SiC vary significantly due to differences in specimen preparation, testing methods, and testing conditions, with one major influence being the indentation size effect (ISE). The ISE results in a trend of decreasing measured hardness with increasing indentation load up to a plateau. Swab [49] found the Knoop hardness to be load-independent at 1 kgf Knoop or higher for many common armor ceramics. Vargas-Gonzalez et al. [1] studied the ISE for B_4C and SiC and found both Knoop and Vickers measured hardness to vary with load up to 2 kgf.

Fig. 10 summarizes Knoop indentation hardness results for the (A) discrete and (B) continuous specimens, which were collected consistent to the 2 kgf standard prescribed in ASTM C1327 to avoid the ISE. No significant change in hardness was detected between B_4C, SiC, and interface regions in the discrete specimen, which had HK2 and standard deviation values of 21.44 ± 0.74, 21.29 ± 0.42, and 21.26 ± 0.34 GPa, respectively. The larger standard deviation in hardness values measured for the B_4C layers is likely due to the presence of cracks; while residual stress is zero at crack surfaces, tensile stresses are likely still present in uncracked material. For the continuous specimen, indents made in regions with nominal composition ratios of 10–90 vol% B_4C had hardness values of 21.53 ± 0.33 GPa, while indents in regions with nominal compositions closer to pure SiC or B_4C had HK2 values of 20.85 ± 0.31 GPa. Knowing the hardness of B_4C exceeds that of SiC, one could expect the hardness to decrease with increasing SiC content. However, looking at Fig. 10, hardness gradually increases with SiC content until about 4 mm, where it then decreases towards pure SiC. The trend observed is hypothesized to be due to two factors: (1) softening in regions of pure B_4C and SiC due to edge-effects and (2) thermally-induced residual stresses due to composition variation. Based on CTE calculations, B_4C-rich regions will tend towards tensile residual stress, which would decrease hardness, and SiC-rich regions will be under compressive stress, which would increase hardness. However, past 4 mm, the hardness of the nominally pure SiC decreases as residual stresses are partially relieved due to cracking.

A challenge in measuring the hardness of these printed specimens was the presence of large inclusions (hundreds of micrometers), which were of similar size as the indenter tip. Thus, indents made in a B_4C layer may be over the matrix region, a B_4C inclusion, or even a SiC inclusion. Knoop hardness values for the printed B_4C–SiC specimens were within one standard deviation of HK2 values for fully-dense, monolithic B_4C (21.7 ± 0.9 GPa) and SiC (20.6 ± 0.2 GPa) materials reported by Vargas-Gonzalez et al. [1].

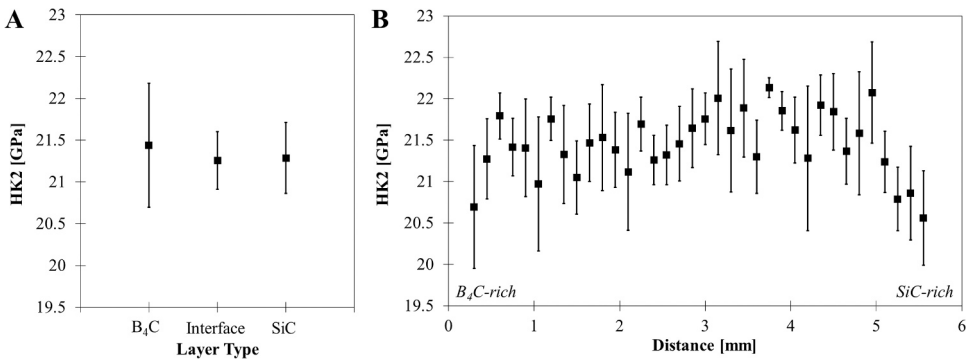

Fig. 10. Knoop indentation hardness data collected for the (A) discrete and (B) continuous B_4C-SiC specimens. All indentations were collected consistent to the 2 kgf standard prescribed in ASTM C1327 to avoid the ISE. Error bars indicate ± one standard deviation.

4. Conclusion

Multi-phase carbide parts were formed via DIW using a custom-built system with multi-material and active in-line mixing capabilities. B_4C and SiC were printed as aqueous ink formulations with high ceramic content and yield-pseudoplastic rheology. The flow behavior of B_4C and SiC inks, having identical ceramic content, was matched across relevant shear rates through the addition of high viscosity methylcellulose. Active, in-line mixing enabled the successful fabrication of discrete and continuous specimens; demonstrating the capability to create both gradual and discrete composition variations in real-time. High-shear mixing achieved by the auger produced micrometer scale mixtures, observed as matrix regions, as well as B_4C and SiC inclusions of sizes tens to hundreds of micrometers. Near full density was achieved for heterogeneous carbide specimens via hot pressing. Cross-sections of densified parts show intimate layer bonding and no printing artifacts. Minimal cracking observed in the continuous specimen reveals that a gradual composition variation reduces residual stress from CTE mismatch, as compared with discrete variations. Residual stress calculations support microstructural observations, where cracking occurs in the B_4C layers due to tensile stress. The hardness of printed B_4C–SiC specimens approximately matched or exceeded that of traditionally processed carbide ceramics. These results indicate the feasibility of tailoring the structure of advanced ceramics through multi-material additive manufacturing.

In the current study, heterogeneity was only tailored in the build direction, or z-direction. Although the custom DIW system is capable of producing heterogeneity in the build plane, or x- and y-direction, two challenges were faced when tailoring composition within a layer. First, purging the material inside the barrel many times during a single layer would waste a significant amount of material. Second, the 'R' modifier is manually added into G-code files so it would be difficult to do this for specific locations, as compared to adding a command just before a layer change. In future work, the 'R' modifier will be automatically added through a custom macro in the Slic3r. In addition, the lag volume will be reduced by optimizing the barrel and auger geometries, which will enable quicker composition changes. Increasing the complexity of heterogeneity will open up additional opportunities for future work, including printing bioinspired structures such as a bouligand arrangement of alternating B_4C and SiC traces [8]. In addition, the printing of discrete specimens with different layer thickness ratios will allow for a cracking spacing study with several datapoints at different residual stresses. The evaluation of these stresses can inform the production of crack-free discrete specimens by calculating an optimal layer thickness ratio.

CRediT authorship contribution statement

Joshua S. Pelz: Methodology, Software, Formal analysis, Investigation, Resources, Data curation, Writing - original draft, Writing - review and editing, Visualization. **Nicholas Ku:** Methodology, Formal analysis, Investigation, Resources, Data curation, Writing - review and editing. **William T. Shoulders:** Formal analysis, Investigation. **Marc A. Meyers:** Methodology, Resources, Writing - review & editing, Supervision, Project administration, Funding acquisition. **Lionel R. Vargas-Gonzalez:** Conceptualization, Methodology, Resources, Writing - review & editing, Supervision, Project administration, Funding acquisition.

Declaration of Competing Interest

The authors declare that they have no known competing financial interests or personal relationships that could have appeared to influence the work reported in this paper.

Acknowledgments

The authors would like to thank the members of the Ceramic and Transparent Materials Branch at the US CCDC Army Research Laboratory, Aberdeen Proving Grounds, MD, specifically Dr. Kristopher Behler and Dr. Michael Kornecki for their technical advice. Also, the authors want to acknowledge Samuel Figueroa, a member of the Meyers group at UCSD, for his efforts in calibrating the custom DIW system.

This research was sponsored by the U.S. Army Combat Capabilities Development Command Army Research Laboratory and was accomplished under Cooperative Agreement Number W911NF-19-2-0054. The views and conclusions contained in this document are those of the authors and should not be interpreted as representing the official policies, either expressed or implied, of the CCDC Army Research Laboratory or the U.S. Government. The U.S. Government is authorized to reproduce and distribute reprints for Government purposes notwithstanding any copyright notation herein.

Funding was supplemented by the UCSD Center for High Energy Density Science (UCOP LAB FEES GRANT ID: LFR-17-449059).

References

[1] L. Vargas-Gonzalez, R.F. Speyer, J. Campbell, Flexural strength, fracture toughness, and hardness of silicon carbide and boron carbide armor ceramics, Int. J. Appl. Ceram. Technol. 7 (2010) 643–651, https://doi.org/10.1111/j.1744-7402.2010.02501.x.

[2] S. Das, W. Ronan, H.N.G. Wadley, V.S. Deshpande, Penetration of confined ceramics targets, Extrem. Mech. Lett. 18 (2018) 45–57, https://doi.org/10.1016/j.eml.2017.11.001.

[3] A. Krell, E. Strassburger, Order of influences on the ballistic resistance of armor ceramics and single crystals, Mater. Sci. Eng. A 597 (2014) 422–430, https://doi.org/10.1016/j.msea.2013.12.101.

[4] W.D. Callister, Materials science and engineering: an introduction (2nd edition), Mater. Des. 12 (1991) 59, https://doi.org/10.1016/0261-3069(91)90101-9.

[5] M.I. Lopez, P.E. Meza Martinez, M.A. Meyers, Organic interlamellar layers, mesolayers and mineral nanobridges: contribution to strength in abalone (Haliotis

rufescence) nacre, Acta Biomater. 10 (2014) 2056–2064, https://doi.org/10.1016/j.actbio.2013.12.016.
[6] M.A. Meyers, A.Y.M. Lin, P.Y. Chen, J. Muyco, Mechanical strength of abalone nacre: role of the soft organic layer, J. Mech. Behav. Biomed. Mater. 1 (2008) 76–85, https://doi.org/10.1016/j.jmbbm.2007.03.001.
[7] W. Yang, B. Gludovatz, E.A. Zimmermann, H.A. Bale, R.O. Ritchie, M.A. Meyers, Structure and fracture resistance of alligator gar (Atractosteus spatula) armored fish scales, Acta Biomater. 9 (2013) 5876–5889, https://doi.org/10.1016/j.actbio.2012.12.026.
[8] V.R. Sherman, H. Quan, W. Yang, R.O. Ritchie, M.A. Meyers, A comparative study of piscine defense: The scales of Arapaima gigas, Latimeria chalumnae and Atractosteus spatula, J. Mech. Behav. Biomed. Mater. 73 (2017) 1–16, https://doi.org/10.1016/j.jmbbm.2016.10.001.
[9] W. Yang, I.H. Chen, B. Gludovatz, E.A. Zimmermann, R.O. Ritchie, M.A. Meyers, Natural flexible dermal armor, Adv. Mater. 25 (2013) 31–48, https://doi.org/10.1002/adma.201202713.
[10] B. Malmal Moshtaghioun, A.L. Ortiz, D. Gómez-García, A. Domínguez-Rodríguez, Toughening of super-hard ultra-fine grained B4C densified by spark-plasma sintering via SiC addition, J. Eur. Ceram. Soc. 33 (2013) 1395–1401, https://doi.org/10.1016/j.jeurceramsoc.2013.01.018.
[11] C. an Wang, Y. Huang, Q. Zan, H. Guo, S. Cai, Biomimetic structure design – a possible approach to change the brittleness of ceramics in nature, Mater. Sci. Eng. C 11 (2000) 9–12, https://doi.org/10.1016/S0928-4931(00)00133-8.
[12] R.P. Wilkerson, B. Gludovatz, J. Watts, A.P. Tomsia, G.E. Hilmas, R.O. Ritchie, A study of size effects in bioinspired, "nacre-like", metal-compliant-phase (nickel-alumina) coextruded ceramics, Acta Mater. 148 (2018) 147–155, https://doi.org/10.1016/j.actamat.2018.01.046.
[13] M.P. Rao, A.J. Sánchez-Herencia, G.E. Beltz, R.M. McMeeking, F.F. Lange, Laminar ceramics that exhibit a threshold strength, Science (286) (1999) 102–105, https://doi.org/10.1126/science.286.5437.102 (80-.).
[14] M. Lugovy, V. Slyunyayev, N. Orlovskaya, G. Blugan, J. Kuebler, M. Lewis, Apparent fracture toughness of Si3N4-based laminates with residual compressive or tensile stresses in surface layers, Acta Mater. 53 (2005) 289–296, https://doi.org/10.1016/j.actamat.2004.09.022.
[15] C.B. Carter, G. Norton. Ceramic Materials: Science and Engineering, 1st ed., Springer, 2007 https://doi.org/10.1007/978-1-4614-3523-5.
[16] V.L. Wiesner, J.P. Youngblood, R.W. Trice, Room-temperature injection molding of aqueous alumina-polyvinylpyrrolidone suspensions, J. Eur. Ceram. Soc. 34 (2014) 453–463, https://doi.org/10.1016/j.jeurceramsoc.2013.08.017.
[17] S. Tariolle, C. Reynaud, F. Thévenot, T. Chartier, J.L. Besson, Preparation, microstructure and mechanical properties of SiC-SiC and B 4C-B4C laminates, J. Solid State Chem. 177 (2004) 487–492, https://doi.org/10.1016/j.jssc.2003.02.007.
[18] N. Travitzky, A. Bonet, B. Dermeik, T. Fey, I. Filbert-Demut, L. Schlier, T. Schlordt, P. Greil, Additive manufacturing of ceramic-based materials, Adv. Eng. Mater. 16 (2014) 729–754, https://doi.org/10.1002/adem.201400097.
[19] M.L. Griffith, J.W. Halloran, Freeform fabrication of ceramics via stereolithography, J. Am. Ceram. Soc. 79 (1996) 2601–2608, https://doi.org/10.1111/j.1151-2916.1996.tb09022.x.
[20] E. Peng, D. Zhang, J. Ding, Ceramic robocasting: recent achievements, potential, and future developments, Adv. Mater. 30 (2018) 1–14, https://doi.org/10.1002/adma.201802404.
[21] N. Oxman, S. Keating, E. Tsai, Functionally graded rapid prototyping, Innov. Dev. Virtual Phys. Prototyp. (2012) 483–489, https://doi.org/10.1201/b11341-78.
[22] ISO/ASTM 52900, Standard Terminology for Additive Manufacturing Technologies – General Principles – Terminology, ASTM B. Stand. i, 2015, pp. 1–9. ⟨https://doi.org/10.1520/ISOASTM52900-15⟩.
[23] J.E. Smay, S.S. Nadkarni, J. Xu, Direct writing of dielectric ceramics and base metal electrodes, Int. J. Appl. Ceram. Technol. 4 (2007) 47–52, https://doi.org/10.1111/j.1744-7402.2007.02118.x.
[24] W. Li, A.J. Martin, B. Kroehler, A. Henderson, T. Huang, J. Watts, G.E. Hilmas, M.C. Leu, Fabricating functionally graded materials by ceramic on-demand extrusion with dynamic mixing, in: Proceedings of the 29th Annual International Solid Freeform Fabrication Symposium – An Additive Manufacturing Conference, 2018, pp. 1087–1099. ⟨http://sffsymposium.engr.utexas.edu/sites/default/files/2018/088⟩. FabricatingFunctionallyGradedMaterialsbyCeram.pdf.
[25] T.J. Ober, D. Foresti, J.A. Lewis, Active mixing of complex fluids at the microscale, Proc. Natl. Acad. Sci. USA 112 (2015) 12293–12298, https://doi.org/10.1073/pnas.1509224112.
[26] D.T. Nguyen, T.D. Yee, N.A. Dudukovic, K. Sasan, A.W. Jaycox, A.M. Golobic, E. B. Duoss, R. Dylla-Spears, 3D printing of compositional gradients using the microfluidic circuit analogy, Adv. Mater. Technol. 4 (2019) 1–7, https://doi.org/10.1002/admt.201900784.
[27] G.V. Franks, C. Tallon, A.R. Studart, M.L. Sesso, S. Leo, Colloidal processing: enabling complex shaped ceramics with unique multiscale structures, J. Am. Ceram. Soc. 100 (2017) 458–490, https://doi.org/10.1111/jace.14705.
[28] J.A. Lewis, Colloidal processing of ceramics, J. Am. Ceram. Soc. 83 (2004) 2341–2359, https://doi.org/10.1111/j.1151-2916.2000.tb01560.x.
[29] L.M. Rueschhoff, Novel Ceramic Near-Net Shaped Processing, 2017.
[30] F.F. Lange, Powder processing science and technology for increased reability, J. Am. Ceram. Soc. 72 (1989) 3–15.
[31] J. Zhou, Y. Zhang, J.K. Chen, Numerical simulation of random packing of spherical particles for powder-based additive manufacturing, J. Manuf. Sci. Eng. Trans. ASME 131 (2009) 0310041–0310048, https://doi.org/10.1115/1.3123324.
[32] H.M. Chan, Layered ceramics: processing and mechanical behavior, Annu. Rev. Mater. Sci. 27 (1997) 249–282, https://doi.org/10.1146/annurev.matsci.27.1.249.
[33] S.L. Morissette, J.A. Lewis, J. Cesarano, D.B. Dimos, T.Y. Baer, Solid freeform fabrication of aqueous alumina-poly(vinyl alcohol) gelcasting suspensions, J. Am. Ceram. Soc. 83 (2000) 2409–2416, https://doi.org/10.1111/j.1151-2916.2000.tb01569.x.
[34] L. Rueschhoff, W. Costakis, M. Michie, J. Youngblood, R. Trice, Additive manufacturing of dense ceramic parts via direct ink writing of aqueous alumina suspensions, Int. J. Appl. Ceram. Technol. 13 (2016) 821–830, https://doi.org/10.1111/ijac.12557.
[35] M. Faes, H. Valkenaers, F. Vogeler, J. Vleugels, E. Ferraris, Extrusion-based 3D printing of ceramic components, Proc. CIRP 28 (2015) 76–81, https://doi.org/10.1016/j.procir.2015.04.028.
[36] J. Liao, H. Chen, H. Luo, X. Wang, K. Zhou, D. Zhang, Direct ink writing of zirconia three-dimensional structures, J. Mater. Chem. C 5 (2017) 5867–5871, https://doi.org/10.1039/c7tc01545c.
[37] D. Zhang, E. Peng, R. Borayek, J. Ding, Controllable ceramic green-body configuration for complex ceramic architectures with fine features, Adv. Funct. Mater. 29 (2019) 1–12, https://doi.org/10.1002/adfm.201807082.
[38] W.J. Costakis, L.M. Rueschhoff, A.I. Diaz-Cano, J.P. Youngblood, R.W. Trice, Additive manufacturing of boron carbide via continuous filament direct ink writing of aqueous ceramic suspensions, J. Eur. Ceram. Soc. 36 (2016) 3249–3256, https://doi.org/10.1016/j.jeurceramsoc.2016.06.002.
[39] S. Eqtesadi, A. Motealleh, F.H. Perera, P. Miranda, A. Pajares, R. Wendelbo, F. Guiberteau, A.L. Ortiz, Fabricating geometrically-complex B4C ceramic components by robocasting and pressureless spark plasma sintering, Scr. Mater. 145 (2018) 14–18, https://doi.org/10.1016/j.scriptamat.2017.10.001.
[40] Sigma-Aldrich, Methyl Cellulose Product Information Sheet, Saint Louis, Missouri, 1997.
[41] J. Pelz, N. Ku, M. Meyers, L. Vargas-Gonzalez, Additive Manufacturing Utilizing a Novel In-Line Mixing System for Design of Functionally Graded Ceramic Composites, 2019.
[42] C.A. Schneider, W.S. Rasband, K.W. Eliceiri, NIH Image to ImageJ: 25 years of image analysis, Nat. Methods 9 (2012) 671–675, https://doi.org/10.1038/nmeth.2089.
[43] C1326-13(2018), Standard Test Method for Knoop Indentation Hardness of Advanced Ceramics, West Conshohocken, PA, 2018. ⟨https://doi.org/10.1520/C1326-13R18⟩.
[44] O.R. Orlovskaya, Nina M. Lugovy, V. Subbotin, Design and manufacturing B4C-SiC layered ceramics for armor applications, Ceram. Armor Armor Syst. (2003), https://doi.org/10.1002/9781118406793.ch5.
[45] T. Li, E. Al Olevsky, M.A. Meyers, The development of residual stresses in Ti6Al4V-Al3Ti metal-intermetallic laminate (MIL) composites, Mater. Sci. Eng. A 473 (2008) 49–57, https://doi.org/10.1016/j.msea.2007.03.069.
[46] M. Lugovy, N. Orlovskaya, K. Berroth, J. Kuebler, Macrostructural engineering of ceramic-matrix layered composites, Compos. Sci. Technol. 59 (1999) 1429–1437, https://doi.org/10.1016/S0266-3538(98)00183-3.
[47] S. Yarmolenko, J. Shih, M. Chheda, J. Sankar, O. Radchenko, N. Orlovskaya, M. Lugovy, V. Subbotin, J. Adams, Robust design and manufacturing of ceramic laminates with controlled thermal residual stresses for enhanced toughness, J. Mater. Sci. 40 (2005) 5483–5490, https://doi.org/10.1007/s10853-005-1923-x.
[48] F. Thévenot, Boron carbide—a comprehensive review, J. Eur. Ceram. Soc. 6 (1990) 205–225, https://doi.org/10.1016/0955-2219(90)90048-K.
[49] J.J. Swab, Recommendations for determining the hardness of armor ceramics, Int. J. Appl. Ceram. Technol. 1 (2005) 219–225, https://doi.org/10.1111/j.1744-7402.2004.tb00173.x.
[50] J.W. Matthews, A.E. Blakeslee, Defects in epitaxial multilayers, J. Cryst. Growth (1974), https://doi.org/10.1016/s0022-0248(74)80055-2.
[51] T.J. Gosling, S.C. Jain, J.R. Willis, A. Atkinson, R. Bullough, Stable configurations in strained epitaxial layers, Philos. Mag. A Phys. Condens. Matter Struct. Defects Mech. Prop. 66 (1992) 119–132, https://doi.org/10.1080/01418619208201517.
[52] J.H. van der Merwe, Structure of epitaxial crystal interfaces, Surf. Sci. 31 (1972) 198–228, https://doi.org/10.1016/0039-6028(72)90261-0.
[53] G.W. Hollenberg, G. Walther, The elastic modulus and fracture of boron carbide, J. Am. Ceram. Soc. 63 (1980) 610–613, https://doi.org/10.1111/j.1151-2916.1980.tb09845.x.
[54] D.T. Livey, P. Murray, Surface energies of solid oxides and carbides, Am. Ceram. Soc. 39 (1956) 363–372.